

Wavelength-modulation-spectroscopy for real-time, in situ NO detection in combustion gases with a 5.2 μm quantum-cascade laser

X. Chao · J.B. Jeffries · R.K. Hanson

Received: 1 July 2011 / Revised version: 20 October 2011
© Springer-Verlag 2011

Abstract A mid-infrared absorption strategy with calibration-free wavelength-modulation-spectroscopy (WMS) has been developed and demonstrated for real-time, in situ detection of nitric oxide in particulate-laden combustion-exhaust gases up to temperatures of 700 K. An external-cavity quantum-cascade laser (ECQCL) near 5.2 μm accessed the fundamental absorption band of NO, and a wavelength-scanned, $1f$ -normalized WMS with second-harmonic detection (WMS- $2f/1f$) strategy was developed. Due to the external-cavity laser architecture, large nonlinear intensity modulation (IM) was observed when the wavelength was modulated by injection-current modulation, and the IM indices were also found to be strongly wavelength-dependent as the center wavelength was scanned with piezoelectric tuning of the cavity. A quantitative model of the $1f$ -normalized WMS- $2f$ signal was developed and validated under laboratory conditions. A sensor was subsequently designed, built and demonstrated for real-time, in situ measurements of NO across a 3 m path in the particulate-laden exhaust of a pulverized-coal-fired power plant boiler. The $1f$ -normalized WMS- $2f$ method proved to have better noise immunity for non-absorption transmission, than wavelength-scanned direct absorption. A 0.3 ppm-m detection limit was estimated using the R15.5 transition near 1927 cm^{-1} with 1 s averaging. Mid-infrared QCL-based NO absorption with $1f$ -normalized WMS- $2f$ detection shows excellent promise for practical sensing in the combustion exhaust.

1 Introduction

Nitric Oxide (NO), as a constituent of the oxides of nitrogen (NO_x), is one of the important atmospheric pollutants produced in the combustion of fossil fuels [1]. Efforts to optimize the fuel economy as well as to optimize pollution-control devices result in a growing demand for accurate and reliable real-time sensors as an important part of a closed-loop control system. In the electric power industry, traditional continuous emissions monitoring (CEM) instrumentation is mostly based upon sampling methods, which suffer from long response time and possible secondary chemistry in the sampling probes. The location of the CEM devices near the exit of the exhaust stack far from the combustion can result in significant lag time. Many commercial plant applications combine the exhaust from multiple combustors for exhaust cleanup treatments before the CEM. Identification of the malfunctioning combustor from the CEM monitor is not possible. Thus, there is a need for real-time, in situ NO sensors placed up-stream in the combustion exhaust on each combustion unit.

Gas sensors based on tunable-laser-absorption spectroscopy have been proved to be a suitable candidate for combustion monitoring because of their capability to make fast, sensitive, accurate, and in situ measurements for a wide variety of gas conditions even in harsh, real-world environments [2]. The fundamental vibrational absorption band of NO in the mid-IR near 5.2 μm and the $A-X$ electronic transition in the ultraviolet (UV) have been used for decades for combustion research [3–5]. Despite the stronger absorption in the UV, there is significant absorption interference in the UV by the combustion product gases of hydrocarbon fuels, and the scattering interference from particulate is much larger than in the infrared. Most importantly, compared with the complexity of UV lasers, in recent years the quantum-

X. Chao (✉) · J.B. Jeffries · R.K. Hanson
High Temperature Gasdynamics Laboratory, Department
of Mechanical Engineering, Stanford University, Stanford,
CA 94035, USA
e-mail: chaox@stanford.edu
Fax: +650-7231748

cascade lasers (QCL) in the mid-infrared have emerged as viable devices for practical use in utility sensors [6–14].

QCL-based NO measurements have been reported previously using both direct absorption (DA) [6–12], and wavelength-modulation-spectroscopy with second-harmonic detection (WMS-2*f*) [10, 11, 15, 16]. Webber et al. [16] used calibrated WMS-2*f* signals with a quantum-cascade distributed-feedback-laser (QC-DFB) to infer NO concentration and demonstrated detection of NO in the few ppb range using a room temperature 100 m multi-pass cell in diluted exhaust-gas bag samples collected in the vehicle certification process. Hancock et al. [10] measured room temperature, low pressure NO at 140 mTorr in gas cells using a continuous wave (CW), external-cavity quantum-cascade laser (ECQCL), and reported a sensitivity of $8.4 \times 10^{-4} \text{ cm}^{-1} \text{ Hz}^{-1/2}$ with DA, enhanced by a factor of 23 with WMS to $3.7 \times 10^{-5} \text{ cm}^{-1} \text{ Hz}^{-1/2}$. With conventional DFB lasers at shorter wavelengths ($1 \mu\text{m} \sim 3 \mu\text{m}$), the WMS method has long been used for sensitive measurements of small concentrations with its relatively easy band-pass filtering mechanism for noise-rejection [17]. Recently, the combination of laser characterization and a normalization scheme ($1f$ -normalized WMS-2*f*, or WMS-2*f*/ $1f$) enables a calibration-free measurement that is immune to laser intensity fluctuation from non-absorption transmission losses [17–21]. Such a scheme would be especially useful in difficult, practical environments, where on-site calibration is often not possible, and particle scattering introduces large noise from fluctuations in the transmitted laser power.

Here we discuss the extension of the calibration-free $1f$ -normalized WMS-2*f* strategy to mid-infrared absorption sensors using an ECQCL. A CW ECQCL at $5.2 \mu\text{m}$ previously purchased to access the R-branch of the first fundamental band of NO for survey measurements to select the best transitions [12] was used here. Previous DA measurements using this laser demonstrated successful in situ monitoring of NO concentration at the economizer exit of a pulverized-coal-fired power plant. In this paper, the transition R15.5 near 1927 cm^{-1} , selected previously [12] as one of the optimum candidates based on relatively low water interference and better laser performance, was used to demonstrate the WMS strategy. Characterization of the laser modulation behavior and the details of the modulation strategy are discussed in Sect. 2. Laboratory validation of the NO measurements is reported in Sect. 3 for a 17.3-cm-long cell filled with calibrated NO mixtures, and for a 1.79-m-long laboratory facility fed by combustion exhaust gases. Finally, Sect. 4 reports the demonstration of performance of the QCL-based WMS sensor in the economizer exhaust of a coal-fired boiler at an electric utility. Variation of the NO concentration was observed as the urea injection for the selective non-catalytic reduction (SNCR) NO_x control was varied. To the author's knowledge, this was the first

Table 1 Wavelength tuning mechanisms of a CW ECQCL

	Grating rotation	Piezoelectric element	Laser injection current
Tuning mechanism	Rotation of the internal diffraction grating	Piezoelectric element installed in the drive train to mechanically modulate the grating	Modulate current through driver board bias-T and change wavelength via laser heating
Driving function	Linear	Sinusoidal	Sinusoidal
Frequency	$\sim 0.2 \text{ Hz}$	$\leq 100 \text{ Hz}$	$10 \text{ kHz} \sim 2 \text{ MHz}$
Tuning range	$\sim 50 \text{ cm}^{-1}$	$\sim 1 \text{ cm}^{-1}$	$\sim 0.05 \text{ cm}^{-1}$

demonstration of a calibration-free $1f$ -normalized WMS-2*f* strategy using an ECQCL architecture. In addition, this was the first real-time, in situ NO monitoring using absorption spectroscopy in a coal-fired power plant boiler. Comparison of the sensor performance with the previous DA measurements illustrates the potential of the $1f$ -normalized WMS-2*f* strategy for routine NO monitoring in combustion exhaust.

2 Laser absorption theory and sensor design

2.1 Modulation characteristics of ECQCL

Before discussing how the WMS signal varies with NO concentration, the wavelength-scanned and wavelength-modulation characteristics of the ECQCL must be discussed. The laser used for these experiments was a commercial (Daylight Solutions) ECQCL that could be tuned “mode-hop-free” from 1895 cm^{-1} to 1951 cm^{-1} ($5.1256 \mu\text{m} \sim 5.2770 \mu\text{m}$). This region spans twenty pairs of NO absorption transitions in the R-branch of its fundamental vibrational band (R5.5~R24.5). The laser outputs a single-mode, CW, collimated beam with a waist size $< 0.5 \text{ mm}$ and a spectral linewidth specified to be $< 0.0015 \text{ cm}^{-1}$. Thus the laser can be treated as a monochromatic light source for the NO spectroscopic measurements.

There are three mechanisms to tune the output wavelength of this laser (grating rotation, piezo-element tuning, and injection-current modulation), and the main characteristics for each are summarized in Table 1. The grating scan of the external-cavity laser provided the ability to conduct a broad-spectrum survey to study both a large number of NO lines and the background water interference for the purpose of optimum line selection. This preliminary work was reported previously [12]. The absorption SNR was improved with faster scanning over shorter wavelength ranges using the piezoelectric element scan. The piezoelectric element was driven by an external PZT controller (Thorlabs

MDT694A) with a sinusoidally varying voltage between 0 and 100 V, and the resulting wavelength scan range was sufficient for scans over a single NO transition. The frequency of this mechanical tuning mechanism, however, is limited to 100 Hz, and waveforms other than the sinusoid are not possible. Finally, higher-frequency modulation can be achieved by sending a sinusoidal driving voltage through the driver board bias-T to add modulation to the injection current. The injection-current tuning of the QC wavelength is mainly accomplished through heating effects as QCLs do not exhibit the plasma dispersion required for the injection-current tuning of conventional diode lasers. Simultaneous with the laser frequency (wavelength) modulation (FM), the laser output also incorporates intensity modulation (IM) at the modulation frequency due to the slope of the local gain where the laser wavelength is set. This non-zero IM offers the opportunity to develop a $1f$ -normalized WMS- $2f$ strategy, which will be discussed in detail in the next section. The measurements reported here used scanned-wavelength WMS using low-frequency piezoelectric scans concurrent with the injection-current modulation.

Due to the limited mechanical precision in the grating-tuning mechanism of this external-cavity laser, fine tuning of the laser wavelength needs to be done by adjusting the piezo-element. For fixed-wavelength measurements, the piezo voltage depended on the position of the grating and thus was different each time the laser grating was adjusted. As a result, the initial setting of the target wavelength without using a wavemeter or reference gas cell was difficult for any fixed-wavelength scheme, especially for field applications. Therefore, scanned-wavelength schemes were selected for the power plant measurements reported here.

Scanned-wavelength WMS for an ECQCL is complicated by the variation of cavity length when the piezo-element drives the grating to tune the laser wavelength. The change in cavity length and imperfect antireflective coatings on the surfaces in the cavity produce constructive and destructive interference, and a varying output intensity exhibits an “etalon” interference pattern. This intensity modulation due to the intra-cavity etalon was approximately $\pm 5\%$. This produced a strongly wavelength-dependent variation in laser IM characteristics. Therefore, to achieve calibration-free detection with $1f$ -normalized WMS- $2f$ using the external-cavity laser, the characterization strategy must account for these IM features.

2.2 Laser absorption theory and $1f$ -normalized WMS- $2f$ techniques

Fundamentals of the laser absorption theory and the WMS technique are briefly reviewed here to define terms and guide the discussion. The author refers the readers to Refs. [17–21] for more details on WMS theory. Optical absorption diagnostics are based upon the Beer-Lambert law shown in (1),

which describes the wavelength-dependent transmission of narrowband light $\tau(\nu)$ as a function of the physical properties (e.g., temperature T , pressure P , and mole fraction χ_i) of the absorbing gas media i . I and I_0 are the transmitted and incident light intensity, respectively, S as a function of T is the temperature-dependent line strength of an isolated absorption transition, ϕ_ν the lineshape function, L the optical path length, and the product $\alpha_\nu = S_T P \chi_i \phi_\nu L$ is often referred to as absorbance.

$$\tau(\nu) = \frac{I}{I_0} \Big|_\nu = \exp(-S_T P \chi_i \phi_\nu L) = \exp(-\alpha_\nu) \quad (1)$$

With a scanned-wavelength DA scheme, the laser output wavelength is swept across the absorption transition and the transmitted laser intensity variation is recorded versus laser wavelength. The lineshape function ϕ_ν is normalized such that $\int_{\text{line}} \phi_\nu d\nu \equiv 1$, and the integrated absorbance area $A = \int_{\text{line}} \alpha_\nu d\nu = S_T P \chi_i L$ can be used to obtain the gas concentration when S , P and L are known or can be reasonably estimated. Note that with this detection method, the light intensity versus laser wavelength without absorption, often referred to as the DA background, must be known to determine the fraction of light transmitted. When an isolated absorption transition is completely scanned, the non-absorption laser intensity is determined by fitting the transmitted intensity from either side of the transition. However, this background intensity is difficult to measure or estimate in a real-field measurement due to the time-varying level of scattering or beam-steering losses. This is exacerbated by the complex variation in laser intensity as the external-cavity architecture is tuned [12].

The scanned-wavelength WMS strategy involves adding a higher-frequency modulation sine wave to the slower-frequency laser tuning. Thus, the laser intensity I_0 and output frequency ν both vary at the modulation frequency (IM and FM, respectively) with the potential for a phase shift between IM and FM and the existence of higher harmonic (nonlinear) terms. This general case can be expressed in a Fourier series as

$$\nu(t) = \bar{\nu}(t) + a \cos(2\pi f_m t) + \dots \quad (2)$$

$$I_0(t) = \bar{I}_0(t) \left[1 + \sum_{n=1}^{\infty} i_n \cos(2\pi n f_m t + \phi_n) \right] \quad (3)$$

where $\bar{\nu}$ and \bar{I}_0 are the center frequency of the slower wavelength scan and intensity at this center wavelength while the laser is modulated at frequency f_m . The modulation indices a, i_n 's and the IM/FM phase shifts ϕ_n 's are laser-specific parameters that are unrelated to the gas absorption properties. In previous studies for the injection-current tuning of a conventional (DFB) diode lasers, only the first-order term in FM and the first- and second-order IM terms were needed to

characterize the small nonlinearity of injection-current tuning of these devices [18]. However, the ECQCL used here required higher-order terms to characterize the laser FM and IM. As ν is modulated, the transmission τ as a function of ν also becomes a periodic function at f_m , and can thus be expanded as

$$\tau[\nu(t)] = H_0 + \sum_{n=1}^{\infty} H_n \cos(2\pi n f_m t) \quad (4)$$

Therefore, in the Fourier space of the transmitted signal $I(t) = I_0(t)\tau(t)$, the presence of the absorption feature will generate nonlinearity in the intensity modulation, and thus produce an absorption-induced signal at frequency $2f_m$. Passing this signal through a lock-in amplifier isolates this second-harmonic signal, from which gas properties can be retrieved. The WMS method shifts the detection bandpass to higher frequency, providing better noise rejection that improves the detectivity compared to scanned-DA.

As can be seen from (3) and (4), the modulated laser intensity is proportional to the center laser intensity $\bar{I}_0(t)$, whereas the transmission $\tau(t)$ only depends on gas absorption properties and laser FM characteristics. The transmitted signal $I(t) = I_0(t)\tau(t)$ is proportional to $\bar{I}_0(t)$, hence all the harmonic components are proportional to $\bar{I}_0(t)$. Taking the ratio of two of the harmonics would then produce a quantity that is independent of the laser intensity, but carries information about gas absorption. When quantitative relationships can be established between this ratio and the gas properties through pre-measured laser FM/IM characteristics and spectroscopic parameters, a calibration-free method is achieved.

For the best signal-to-noise ratio (SNR), the first-harmonic ($1f$) signal is used to normalize the other harmonics, which are extracted by lock-in amplifiers. Note that a non-zero linear IM of the laser is needed for this normalization scheme. Unknown non-absorption factors such as the detector gain or the laser intensity loss by scattering or dusty windows can be canceled out. Signal detection at $1f$ and $2f$ frequencies eliminates uncertainties from a dc drift from broadband background emission or detector background drifts.

Because of nonlinearities in the laser intensity response to a driving signal, the $2f$ signal will be non-zero in the absence of gas absorption. This background signal is often called the residual amplitude modulation (RAM), and will be subtracted here from the total $2f/1f$ signal to produce the absorption-induced signal.

2.3 Characterization of laser modulation parameters

To calculate the expected WMS- $2f/1f$ spectrum, the laser modulation behavior needs to be fully characterized to reproduce an accurate simulation. These characteristics must be understood to optimize the modulation parameters to

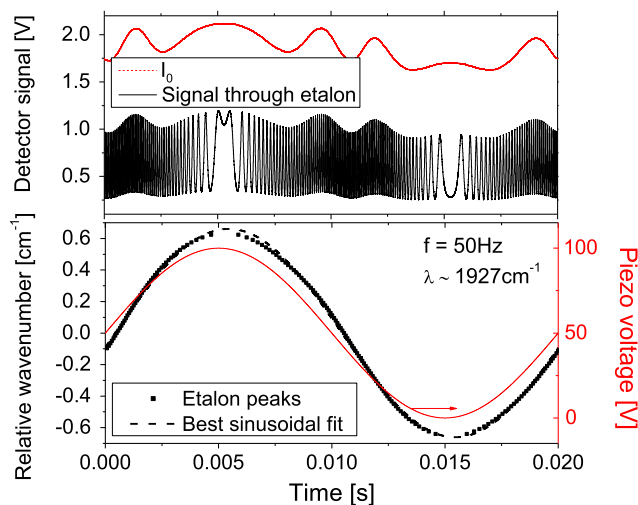


Fig. 1 Piezoelectric scan intensity and wavelength variation at 50 Hz near 1927 cm^{-1}

achieve the best SNR. The effects of modulation frequency and driving source voltage on the IM and FM indices for both the piezo scan and the current modulation are characterized below, first separately, and then combined as scanned-wavelength WMS.

For the piezo scans, the PZT controller was driven by an external sinusoidal wave $V_p = \bar{V}_p + V_s \sin(2\pi f_s t)$, where \bar{V}_p is the average voltage, V_s is the scan voltage amplitude, and f_s the scan frequency. Since only positive voltage up to 100 V can be applied to the controller, we set $\bar{V}_p = 50 \text{ V}$, and varied V_s between 0 to 50 V to achieve the required scanning range. Figure 1 shows an example of the laser intensity and wavelength variation recorded at a scanning frequency of 50 Hz and center wavenumber near 1927 cm^{-1} . A solid germanium etalon (free spectral range = 0.016 cm^{-1}) was used to characterize the relative variation of laser frequency by recording the peak position of the interference fringes. As exhibited by the dashed curve in the upper panel, when the piezo-element monotonically changed the cavity length, the output intensity was modulated with an “etalon” pattern. This is similar to what we observed in the wide-range grating-tuning mode, and is typical of the external-cavity laser architecture. The laser output frequency (in wavenumbers), tunes simultaneously such that $\nu_p = \bar{\nu}_p + \nu_s \sin(2\pi f_s t + \phi_s)$, where $2\nu_s$ and ϕ_s characterize the laser frequency scan range and phase shift, respectively. These laser characteristics were measured for different scan frequencies and amplitudes, with results shown in Fig. 2. As a typical result, scanning the laser with a full voltage swing of 0~100 V at 50 Hz yields a laser frequency scan range of $\sim 1.35 \text{ cm}^{-1}$, enough to cover the spin-split doublet pair of NO transitions (from the spin-split ground electronic state $X^2\Pi_{1/2}$, $X^2\Pi_{3/2}$). It was found that for all scan frequencies up to 100 Hz, larger driving voltage amplitudes result in larger scan ranges and phase shifts, and differences

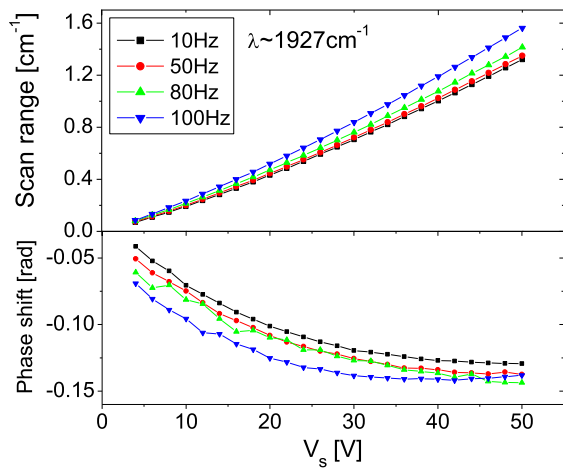


Fig. 2 Piezoelectric scan-wavelength range and phase-shift characterization at different scan frequencies near 1927 cm^{-1}

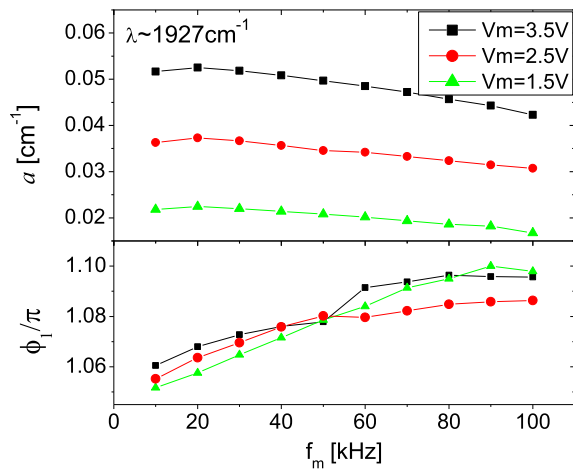


Fig. 3 Current-modulation FM and linear phase shift at different modulation frequencies and driving voltage

between the laser characterization at different scanning frequencies were small. However, the laser was also found to be more prone to mode-hops and intensity instabilities at higher scanning frequencies. Thus the 50 Hz frequency was chosen for the measurements reported here.

The current-modulation behavior was first characterized with a fixed center wavelength, i.e., with $\bar{\nu}$ in (2) constant. The driving voltage was a sinusoidal function about ground at modulation frequency f_m , $V_b = V_m \cos(2\pi f_m t)$, where V_m is the driving voltage amplitude. As shown in Fig. 3, larger V_m yielded larger FM depth, and a maximum V_m of 3.5 V was selected to obtain reasonably large FM amplitude without damaging the laser. As the modulation frequency was increased, a decrease in FM depth and slight rise in phase shift ϕ_1 were observed. Similar to the injection-current modulation of a DFB diode laser, we measured the phase shift between the FM and IM to be slightly over π . Due to limitations imposed by the current-

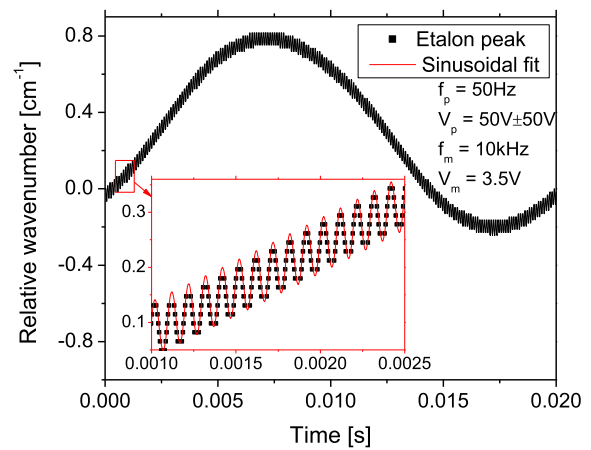


Fig. 4 Laser output wavenumber variation under combined piezoelectric scan at 50 Hz and current modulation at 10 kHz

modulation mechanism, the achievable FM depths were significantly less than the optimum value desired for measurements of atmospheric pressure-broadened lineshapes (optimum a around $2.2 \times \Delta\nu \approx 0.12 \text{ cm}^{-1}$, where $\Delta\nu$ is the half-width-half-maximum (HWHM) of the absorption transition [21, 22]). To maximize the FM depth, modulation parameters of $f_m = 10 \text{ kHz}$ and $V_m = 3.5 \text{ V}$ were selected.

When the piezo scan and current modulation were applied simultaneously, the two mechanisms acted independently without apparent physical interaction with each other. This resulted in a fast modulation superimposed upon a slowly varying center value. The FM under this circumstance was again characterized by passing the laser light through a solid etalon and tracking the interference fringe peaks, and the measured results are shown in Fig. 4. It was observed that the injection-current modulation depth a did not vary with phase of the piezo scan, therefore the laser FM can be characterized as

$$\begin{aligned} \nu &= \nu_p + a \cos(2\pi f_m t) \\ &= \bar{\nu}_p + \nu_s \sin(2\pi f_s t + \phi_s) + a \cos(2\pi f_m t) \end{aligned} \quad (5)$$

On the other hand, the IM indices were found to be strongly wavelength-dependent due to the large curvatures in the baseline produced by the “etalon” pattern. This is significantly different from that observed for the near infrared (NIR) DFB lasers used in previous WMS- $2f/1f$ research [18, 21]. Instead of the single-point characterization for a fixed-wavelength WMS characterization scheme used by Li, et al. [18], the laser signals with simultaneous scanning and modulation were passed through a lock-in amplifier with reference signals at harmonic frequencies nf_m ($n = 1, 2, \dots$), and the background signal at each of the harmonics nf can be obtained by using lock-in amplifiers at each harmonic. These data provide the IM index i_n over the entire scanned wavelength range. Figure 5 shows the

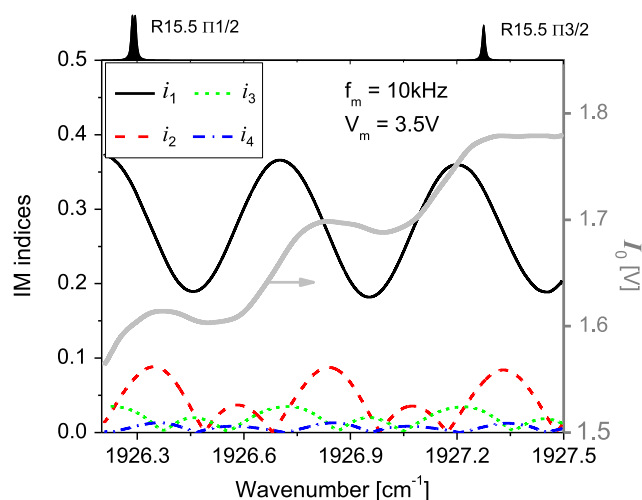


Fig. 5 Laser output IM indices with scanned-WMS scheme at 10 kHz modulation frequency near 1927 cm^{-1}

first four orders of the measured IM indices near the center wavenumber of 1927 cm^{-1} over the range that covers the R15.5 (${}^2\Pi_{1/2}$, ${}^2\Pi_{3/2}$) doublet. All indices oscillated with a period of $\sim 0.5 \text{ cm}^{-1}$ corresponding to the period in the interference fringes of the scanned laser intensity background from the change in cavity length, with a phase shift of $\sim \pi/2$ between consecutive orders as expected from the analogy between Fourier series and Taylor expansion for small modulation amplitudes. Despite the small FM depth, these IM indices were notably larger ($i_1 \sim 0.2\text{--}0.4$) than the typical values for NIR DFB lasers with small modulation depths (e.g., $a = 0.1 \text{ cm}^{-1}$, $i_1 \sim 0.1$). More importantly, due to the large nonlinearity in the intensity background of an ECQCL, the higher-order terms were significant, and were only a factor of 10 smaller than the linear term as compared with the ~ 100 times difference for a typical NIR DFB laser ($i_2 \sim 0.001$). Thus the ECQCL had a much larger background $2f$ signal (RAM). Careful characterization of the modulation indices over the entire wavelength range scanned was necessary for an accurate determination of this background, which was vector-subtracted from the measured WMS- $2f$ signals.

The dependence of the IM and FM indices on the driving voltage V_m was studied and illustrated in Fig. 6 for $f_m = 10 \text{ kHz}$. For the wavelength-dependent i_n 's, the average over a repeating period of $\sim 0.5 \text{ cm}^{-1}$ was taken as the representative value for each V_m . It was found that whereas $a \propto V_m$, the i_n 's can be best characterized as proportional to V_m to the n th power. The largest a possible using V_m of 3.5 V was used even though this value required characterization of the first few orders of nonlinear laser-intensity response.

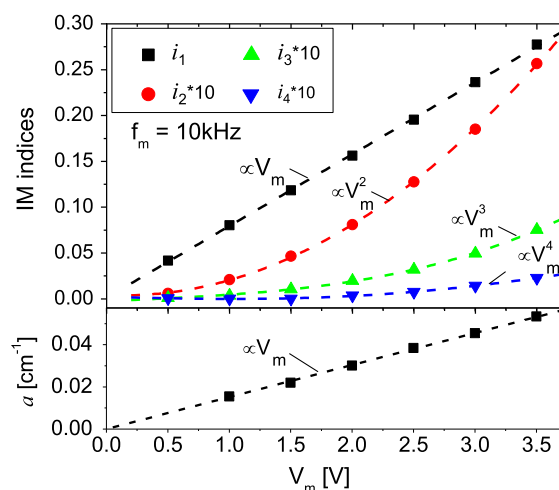


Fig. 6 Laser output IM and FM indices at different driving voltages

3 Laboratory validation of sensor performance

3.1 Static-cell measurements

The characterization of the laser modulation behavior including all the FM/IM indices and phase shifts allowed an accurate simulation of the WMS- $2f/1f$ spectrum for a specific gas condition (T , P , χ_i). Comparing the simulation with the measured spectrum yielded the concentration χ_i when T and P are known. The NO sensor was constructed and validated in a static cell with calibrated mixtures and in a laboratory rig for combustion exhaust.

Pressure-controlled measurements were conducted in a room-temperature static cell with an optical path length of 17.3 cm. The optical and plumbing system setup is shown in Fig. 7. The cell had 2.5-cm-diameter CaF_2 wedged windows, and a wedged ZnSe beam splitter was used to separate a fraction of the laser beam into a matched reference detector. With careful manipulation of the optical alignment to avoid the production of additional etalons in the optical path, the $1f$ -normalized $2f$ signals were independent of the alignment, absolute light intensity, and different detector gains, and were site-independent and calibration-free. Therefore, the WMS- $2f/1f$ magnitudes were the same for both beam paths except for the absorption-generated signals. Thus this reference setup allowed real-time monitoring and subtraction of the WMS- $2f/1f$ background, to produce the absorption-induced WMS- $2f/1f$ magnitudes for gas-sensing purposes without the need to mathematically fit an unknown background. Calibrated NO gas mixtures with accurately known concentrations were used to fill the cell at and below atmospheric pressure, and the total pressures were monitored with a baratron (MKS 627B). The measured WMS- $2f/1f$ lineshapes were validated against the simulation using the given gas parameters.

Fig. 7 Room-temperature static-cell setup with controlled pressure and optical path length of 17.3 cm

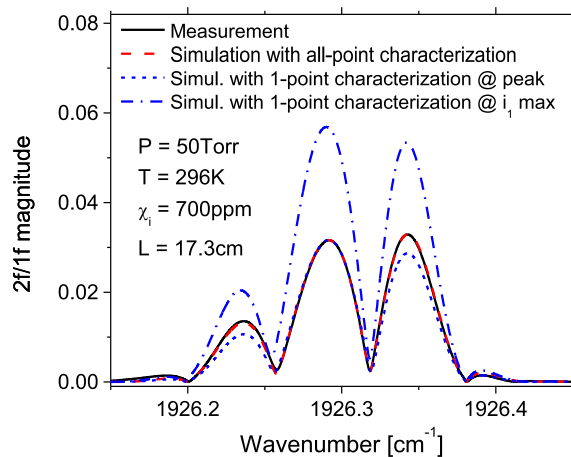
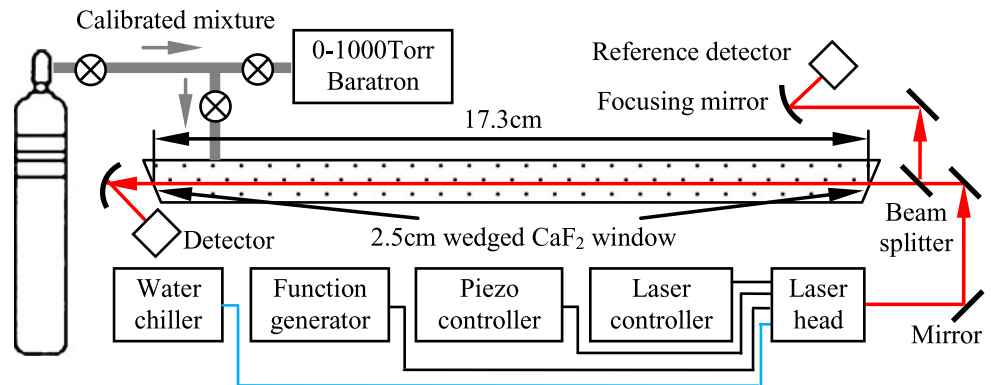


Fig. 8 Validation of measured scanned WMS- $2f/1f$ lineshape for transition R15.5 ($\Pi_{1/2}$) near 1926.3 cm^{-1} in static cell against simulated lineshapes

Figure 8 shows an example of a measured single-sweep WMS- $2f/1f$ lineshape in the cell for the R15.5 ($\Pi_{1/2}$) transition centered near 1926.3 cm^{-1} at a reduced pressure of 50 Torr and concentration of 700 ppm. The measurement was performed with the selected modulation parameters $f_s = 50 \text{ Hz}$, $f_m = 10 \text{ kHz}$, $V_s = 50 \text{ V}$, $V_m = 3.5 \text{ V}$ and compared with the simulated spectrum. The measured result is shown in the plot with black solid line. The simulated lineshape accounting for the wavelength-dependent IM indices such as that shown in Fig. 5, is plotted in the red dashed line. (For the references to color in this figure, the reader is referred to the web version of this paper.) This simulation result matched the entire measured lineshape within 2%, and the center peak value near the transition center matched within 0.25%. With such a simulation scheme, fitting the entire lineshape or picking the peak value are both valid methods to infer the gas concentration. However, it was found that the side peak values were more susceptible to uncertainties in the IM phase shifts than the center peak because of the fact that the odd harmonics of the absorption feature are only zero at line center for isolated transitions (H_1, H_3, \dots in (4)). In addition, the real-time data processing algorithm

was more efficient at selecting the center peak value, and hence the peak value was used to infer gas concentration for the prototype NO sensor.

The effectiveness of the wavelength-scanned all-point characterization scheme to improve the simulation accuracy is illustrated in Fig. 8 by comparison with the simulation results using single-point characterization, i.e., when the wavelength-dependences of the modulation indices are neglected and the i_n 's are fixed as constants for all wavelengths. The simulation shown with the short dashed line still fit the measurement within 1% near the center peak where the fixed i_n 's were taken at, but $\sim 10\%$ error was seen at the two side peaks. With a measurement scheme that uses the center peak value to infer the gas concentration, this simulation method was still able to produce the correct value, keeping in mind that the validity of the measurement depended upon correctly fixing the laser characteristic parameters and identifying the correct peak. The latter can be difficult in cases where absolute wavelengths are unknown, absorption is large, FM depth not optimized, or when the center peak is not the maximum in the scan range. Finally, the extent of error that inaccurate determination of the laser parameters at the corresponding wavelength could introduce is illustrated by simulating the spectrum using the characteristic parameters at 0.2 cm^{-1} away from the line center where i_1 was most different from the line center value. This is shown by the dash-dotted line in Fig. 8; here an error of nearly 80% was observed in the center peak value. This, again, shows the importance and effectiveness of the scanned-wavelength characterization scheme.

The experiment was repeated for a series of gas pressures with the same gas mixture, and measured values are validated against the simulation, as shown in Fig. 9. As discussed above, since the FM index could not be set large enough to achieve the optimum value for atmospheric pressure-broadened line widths, the maximum WMS- $2f/1f$ signal magnitude for a fixed a occurs at a reduced pressure where lines are narrower, e.g., $\sim 350 \text{ Torr}$ for $a = 0.05 \text{ cm}^{-1}$ with $V_m = 3.5 \text{ V}$, and $\sim 200 \text{ Torr}$ for $a = 0.03 \text{ cm}^{-1}$ with $V_m = 2 \text{ V}$. These experimental re-

sults in the static cell validated our WMS model and confirmed the theoretical prediction of optimum modulation depth at $2.2\Delta\nu$.

In the room-temperature cell measurement at 1 atm using a modulation depth of 0.05 cm^{-1} , a SNR of about 1800 was estimated for a single-sweep line shape. This led to a room-temperature, atmospheric pressure detection limit of $\sim 0.07\text{ ppm}\cdot\text{m}$ for the static-cell measurements.

3.2 Laboratory measurements in combustion exhaust

The test rig (Fig. 10) provides a more realistic environment to test the sensor performance in hot combustion flue gas that imitates the real-world combustion exhaust conditions of a practical boiler with abundant ($\sim 10\%$) water vapor mole fraction. The exhaust of an ethylene-air flame was directed through a duct with a uniform-temperature optical path of 1.79 m, which could be maintained at temperatures up to 1000 K. The gas effluent from the flame could be altered by the addition of metered flows of known gas mixtures through the co-flow of the burner and/or injected into

the burned gases above the flame. This approach enabled controlled variation of the NO concentration in the total flow. Water-cooled quartz probes were installed on two ends of the duct to provide traditional extractive sampling measurements using a chemiluminescent NO_x analyzer (Teledyne instruments model 200EH).

A series of experiments was performed in the exhaust test rig at exhaust temperature of 600 K for different levels of NO concentrations over the range of 10 to 100 ppm, and the optical measurement results using the scanned WMS- $2f/1f$ scheme were validated against both the DA and the sampling measurement results (Fig. 11). The results using the three different methods constantly agreed within 5%, with a 2σ uncertainty of 5% of the optical measurement estimated based on the contributions from temperature (2%), pressure (0.5%), gas mixture (3%), and statistical uncertainty of repetitive measurement (2%). A SNR of about 200 was estimated for the lowest concentration level of 12 ppm measured in the above experiment, demonstrating a single-sweep noise-equivalent detection limit of $0.1\text{ ppm}\cdot\text{m}$.

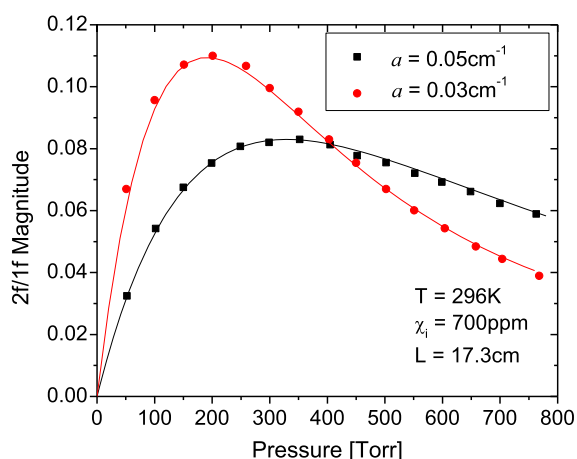


Fig. 9 Validation of measured scanned WMS- $2f/1f$ peak value against simulation at different pressures and FM depths

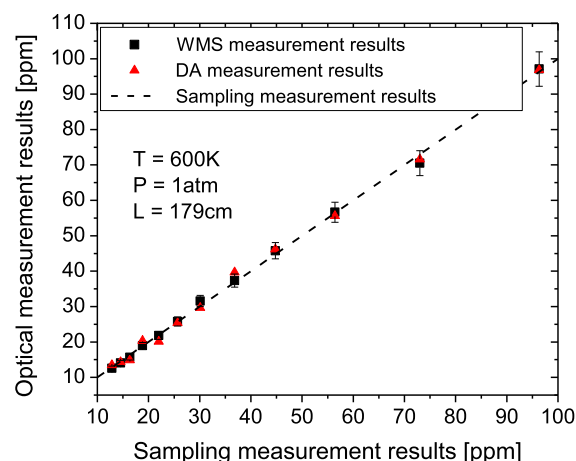
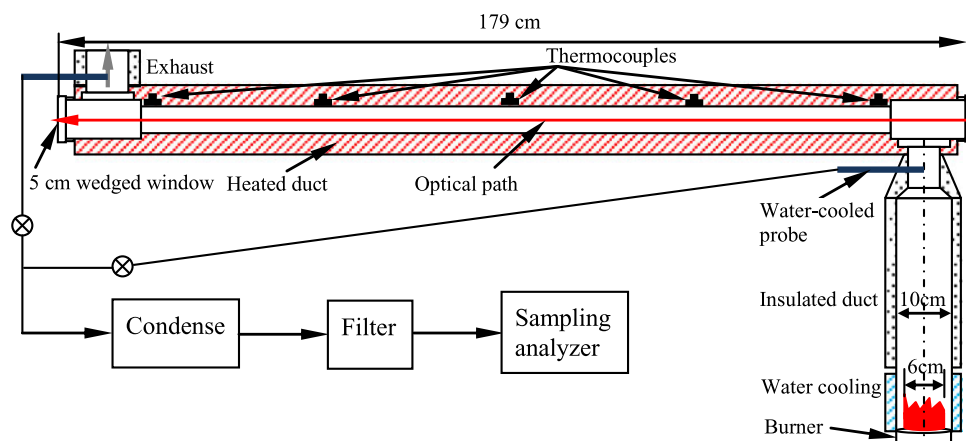


Fig. 11 Measured NO concentrations in combustion-exhaust rig using scanned-wavelength WMS method and comparison with DA and sampling method results

Fig. 10 Combustion-exhaust rig showing laboratory burner, constant-temperature exhaust duct, optical access and gas-sampling ports



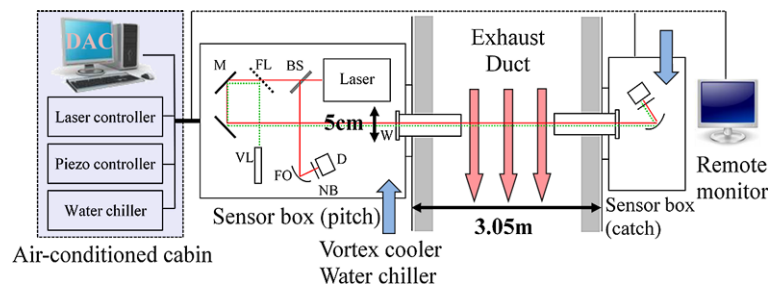


Fig. 12 Sensor setup for field measurement of NO in a coal-fired power plant. Two sensor boxes (pitch and catch sides) are mounted on opposite sides of the duct wall. M, mirror; FL, flipper mirror; BS,

beam splitter; VL, visible laser; FO, focusing mirror; NB, narrow band filter; D, detector; W, window. Solid red line: mid-IR laser beam path; dotted green line: visible laser beam path

4 Real-time NO measurements in coal-fired power plant

4.1 Prototype sensor design and field implementation

We evaluated the field use of the WMS- $2f/1f$ sensor scheme for real-time NO concentration measurement in the combustion exhaust at the economizer exit of a coal-fired power plant. Prototype absorption sensors were designed using the results of our fundamental spectroscopy measurements and the lessons-learned from the laboratory validation experiments discussed above. Real-time, in situ measurements were demonstrated in a 300 MW unit of a 1.2 GW pulverized-coal-fired power plant using the $1f$ -normalized, scanned-wavelength, WMS- $2f$ method. Measurements using only DA were conducted previously and much of the sensor hardware from those experiments was used again here [12]. The temperature at the measurement location was ~ 624 K (660 F), and the pressure inside the duct was slightly below atmosphere (0.978 atm) for safety concerns. Flanged ports were available with a clear line-of-sight across the duct to provide an optical path length of 3.05 m (10 feet) in the central portion of the duct. Figure 12 shows the sensor setup and optical layout, in which two NEMA enclosures mounted onto the flanges housed the laser transmitter and detector optics for mechanical protection and temperature control. A visible green laser beam was used to facilitate alignment of the mid-IR beam in the dark, confined environment of the economizer duct.

In previous work, we demonstrated successful time-resolved, continuous monitoring of NO concentration using DA schemes in this hostile power plant environment with elevated ambient temperatures (above 120 F), significant dust, dirt, and fugitive coal dust. In this second-generation prototype sensor, we improved our system by incorporating the calibration-free WMS method, which proved to be especially advantageous for facile real-time monitoring and enhanced noise-rejection capability. We have also refined our system by replacing the liquid-nitrogen-cooled detectors used previously with thermoelectrically cooled versions

(InfraRed Associates, MCT-5-TE3-1.0-PV(OE)) to improve the practicality of long-term use of such a system in the boiler environment.

4.2 Field measurement results and discussion

The dominant noise sources in the power plant environment included mechanical vibration, time-varying scattering noise and beam steering in the turbulent flow, rather than detector or laser noise. These influences increased the difficulty and uncertainty in determining the non-absorption baseline I_0 required by DA measurements for the external-cavity laser architecture with its complex variation in intensity versus wavelength. These non-absorption laser-intensity fluctuations were, however, accounted for by the $1f$ -normalization strategy, which made the WMS- $2f/1f$ scheme more advantageous. In addition, the normalized WMS strategy was more amenable to real-time data processing. It was found that the normalization reduced the noise from the intensity fluctuations by a factor of about 10 compared to DA, and this observation was illustrated by the raw signal from a single sweep shown in Fig. 13. Note that the intensity of the laser was modulated by a mechanically (piezo) tuned wavelength as illustrated by the scan in the upper panel of Fig. 13, and the variation of the intensity baseline from the reference detector signal is shown in the red dashed line. In the bottom panel is the raw data for a wavelength-scanned WMS- $2f/1f$ signal. Thanks to the normalization scheme, the transmitted WMS signals were not affected by the intensity fluctuations and deviated from the reference signal only where absorption features were present. Real-time vector subtraction of the reference background signal from the transmitted signal produced the absorption-induced WMS spectra shown at the bottom in Fig. 13. Clearly, this approach effectively suppresses the complicated variation of laser intensity with wavelength, and is also free of interference from non-absorption losses. This single-sweep data trace was measured with an NO concentration of 106 ppm, and had a SNR of ~ 175 . This implies a noise-equivalent detection limit with $\text{SNR} = 1$ of 0.6 ppm

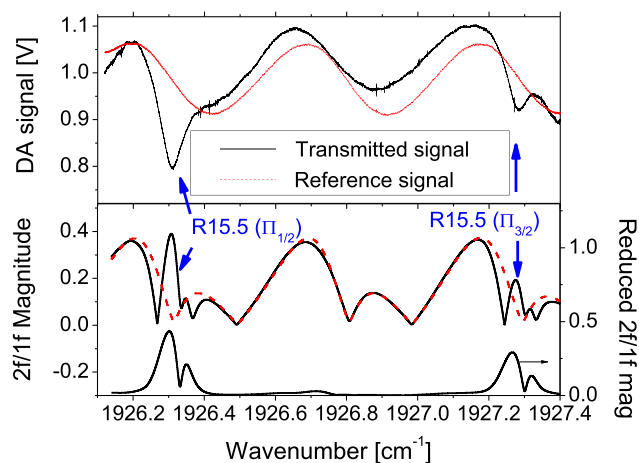


Fig. 13 Comparison of single-sweep raw signal using scanned DA and WMS- $2f/1f$ schemes. Background-subtracted $2f/1f$ magnitude is shown on the right axis in the bottom panel

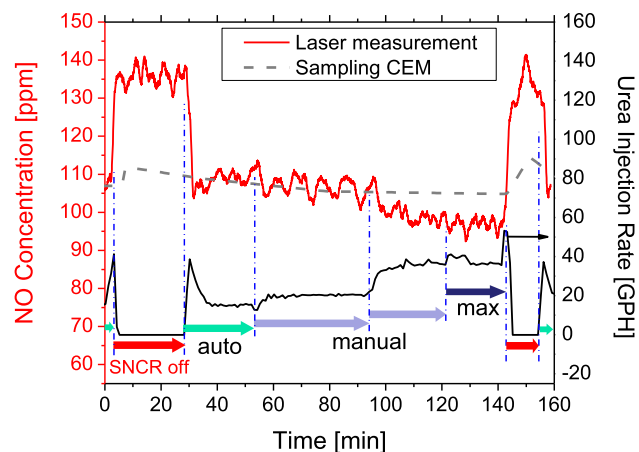


Fig. 14 Real-time optical measurement of NO concentration during variation of the SNCR NO_x control system operation level. The urea injection rate and the CEM data for NO_x ($\text{NO} + \text{NO}_2$) concentration recorded in the exhaust stack are shown for comparison

for the 3 m path length in the boiler exhaust, a value that improved to 0.1 ppm with one-second averaging.

The NO concentration in the boiler flue gas was monitored with the WMS- $2f/1f$ sensor as a function of combustion- and exhaust-gas treatment. Figure 14 shows an example result for a continuous, three-hour measurement using the R15.5 ($\Pi_{1/2}$) transition. During this time window, the urea injection for the SNCR NO_x control system was varied in discrete steps from no added urea, to automatic urea addition, to manual operation with step increases in urea injection and back to no added urea. In Fig. 14 the measured NO concentration in ppm is shown in red, the plant-recorded urea injection rate is shown as a black solid line (values in gallons per hour are shown on the right axis in the plot), and the plant-recorded continuous emission monitoring (CEM) measurements of NO_x ($\text{NO} + \text{NO}_2$) are shown as a gray

dashed line. The laser absorption measurements of NO concentration closely followed the urea injection rate, with increased urea resulting in more NO reduction, and vice versa. In addition to the expected steady changes in NO concentration, transient changes in the NO were also captured, including sharp rises/falls, overshoots, and oscillations. These transient changes were completely overlooked by the sampling CEM measurement; also note the CEM reports NO_x with a delay of several minutes due to the long averaging and sampling times needed for the CEM instrumentation. In addition, the plant CEM also combines the exhaust from several boilers into a single stream before the CEM measurements. The near-instantaneous time response associated with the laser sensor demonstrates the potential for use of such a monitor in a process control function. Note that these data were collected without operator intervention of the sensor optics alignment or adjustment. In this highly successful demonstration, real-time, in situ NO monitoring with ppm sensitivity and sub-second time response was accomplished with improved robustness against non-absorption laser intensity losses compared to the earlier DA measurements in this coal-fired boiler.

5 Conclusions

Characteristics of the modulation behavior with different tuning mechanisms, modulation amplitudes and frequencies of an ECQCL near $5.2 \mu\text{m}$ were investigated to establish an accurate model for scanned-wavelength $1f$ -normalized WMS- $2f$ used for an NO absorption sensor in combustion gases. The IM and FM behavior of the external-cavity laser were characterized to achieve the calibration-free method and select optimum modulation parameters. WMS models were first validated under laboratory conditions with controlled temperature, pressure, and gas concentrations. Scanned-wavelength WMS measurements were performed with 10 kHz current modulation concurrent with 50 Hz piezo scan of the grating, and the R15.5 transition near 1927 cm^{-1} within the $5.2 \mu\text{m}$ NO fundamental band was used to demonstrate the sensor performance. NO was detected in a static cell filled with calibrated NO mixtures, and in a 1.79-m-long uniform-temperature combustion exhaust rig fed by atmospheric-pressure combustion gases from an ethylene flame. The WMS- $2f/1f$ lineshapes measured in the cell over a range of total pressure between 50 Torr and 800 Torr agreed with simulated spectrum within 2%, and measurements in combustion gases at 600 K with NO concentrations between 10 ppm and 100 ppm agreed with DA and sampling measurements within 5%. The sensor was then applied in a field measurement of NO at the exit of the economizer in a coal-fired boiler in an electric utility, where gas temperature was $\sim 624 \text{ K}$. A three-hour continuous measurement of NO during a period of step changes in urea-injection

rate of the SNCR NO_x control system was reported, providing direct evidence of real-time, in situ, unattended observation of transient NO behavior in the boiler exhaust as a function of the SNCR control. The $1f$ -normalized WMS- $2f$ strategy was found to reject fluctuations from mechanical vibration, particulate scattering, and beam steering noise in the boiler environment. A noise-limited detection limit of 0.1 ppm was achieved over the 3 m optical path for 1 s averaging. This successful field demonstration illustrated the potential of this QCL-based mid-infrared sensor for real-time, continuous, in situ monitoring of NO in harsh environments including coal-fired boiler exhaust.

Acknowledgements Support was provided by the Electric Power Research Institute with Mr. Richard Himes as program manager and the Air Force Office of Scientific Research with Dr. Julian Tishkoff as program manager. We thank Dr. Michael Radunsky and Dr. Sam Crivello of Daylight Solutions for their useful comments on an early version of the manuscript.

References

1. US Environmental Protection Agency, National air quality and emissions trends report, Special Studies ed., Sept, 2003, available at <http://www.epa.gov/air/airtrends/aqtrnd03/>
2. R.K. Hanson, Proc. Combust. Inst. **33**, 1 (2011)
3. P.K. Falcone, R.K. Hanson, C.H. Kruger, Combust. Sci. Technol. **35**, 81 (1983)
4. K.C. Smyth, D.R. Crosley, in *Applied Combustion Diagnostics*, ed. by K. Kohse-Höinghaus, J.B. Jeffries (Taylor and Francis, London 2002), pp. 9–68, Chap. 2
5. T.N. Anderson, R.P. Lucht, S. Priyadarsan, K. Annamalai, J.A. Caton, Appl. Optim. **46**, 3946 (2007)
6. J.B. McManus, J.H. Shorter, D.D. Nelson, M.S. Zahniser, D.E. Glenn, R.M. McGovern, Appl. Phys. B **92**, 387 (2008)
7. M.S. Zahniser, D.D. Nelson, J.B. McManus, S.C. Herndon, E.C. Wood, J.H. Shorter, B.H. Lee, G.W. Santoni, R. Jimenez, B.C. Daube, S. Park, E.A. Kort, S.C. Wofsy, Proc. of SPIE **7222**, 72220H (2009)
8. V.L. Kasyutich, R.K. Raja Ibrahim, P.A. Martin, Infrared Phys. Technol. **53**, 381 (2010)
9. V.L. Kasyutich, R.J. Holdsworth, P.A. Martin, J. Phys. Conf. Ser. **157**, 012006 (2009)
10. G. Hancock, J.H. van Helden, R. Peverall, G.A.D. Ritchie, R.J. Walker, Appl. Phys. Lett. **94**, 201110 (2009)
11. Y.A. Bakhirkin, A.A. Kosterev, C. Roller, R.F. Curl, F.K. Tittel, Appl. Optim. **43**, 2257 (2004)
12. X. Chao, J.B. Jeffries, R.K. Hanson, Proc. Combust. Inst. **33**, 725 (2011)
13. A.A. Kosterev, C. Roller, F.K. Tittel, W. Flory, in *OSA/CLEO* (2003)
14. G. Wysocki, A.A. Kosterev, F.K. Tittel, Appl. Phys. B **80**, 617 (2005)
15. B.W.M. Moeskops, S.M. Cristescu, F.J.M. Harren, Optim. Lett. **31**, 823 (2006)
16. W.H. Weber, J.T. Remillard, R.E. Chase, J.F. Richert, F. Capasso, C. Gmachl, A.L. Hutchinson, D.L. Sivco, J.N. Baillargeon, A.Y. Cho, Appl. Spectrosc. **56**, 706 (2002)
17. D.T. Cassidy, J. Reid, Appl. Optim. **21**, 1185 (1982)
18. H. Li, G.B. Rieker, X. Liu, J.B. Jeffries, R.K. Hanson, Appl. Optim. **45**, 1052 (2006)
19. G.B. Rieker, X. Liu, H. Li, J.B. Jeffries, R.K. Hanson, Appl. Phys. B **87**, 169 (2007)
20. G.B. Rieker, J.B. Jeffries, R.K. Hanson, Appl. Phys. B **94**, 51 (2009)
21. G.B. Rieker, J.B. Jeffries, R.K. Hanson, Appl. Optim. **48**, 5546 (2009)
22. J. Reid, D. Labrie, Appl. Phys. B **26**, 203 (1981)